Microneedle–Tissue Interaction Across Varying Biological and Mechanical Conditions

Elham Lori Zoudani , Prabuddha De Saram , Kyle Engel , Nam-Trung Nguyen , Navid Kashaninejad *

Posted Date: 25 June 2025

doi: 10.20944/preprints202506.2067.v1

Keywords: microneedles; tissue adhesion; drug delivery; biosensing; insertion force; extraction force

 doi:10.20944/preprints202506.2067.v1

Article

Microneedle–Tissue Interaction Across Varying Biological and Mechanical Conditions

Elham Lori Zoudani [1], Prabuddha De Saram [1], Kyle Engel [2], Nam-Trung Nguyen [1,*] and Navid Kashaninejad [1,3,*]

[1] Queensland Quantum and Advanced Technologies Research Institute, Griffith University, Australia
[2] Centre for Regional and Rural Futures (CeRRF), Centre for Sustainable Bioproducts (CSB), School of Engineering, Deakin University, Australia
[3] School of Engineering and Built Environment, Griffith University, Australia
* Correspondence: nam-trung.nguyen@griffith.edu.au (N.-T. N); n.kashaninejad@griffith.edu.au (N.K.)

Abstract: Microneedle (MN)–tissue interactions play a critical role in the efficiency and reliability of transdermal drug delivery and biosensing, yet their mechanistic understanding remains limited. This study systematically investigates the effects of biological (tissue type and temperature) and mechanical (needle design, material, and insertion velocity) parameters on the performance of microneedle insertion and extraction. Experiments were performed on porcine skin, chicken breast, and agarose gel to represent varying tissue properties. Additionally, the effect of tissue temperature on replicating physiological conditions, such as hypothermia and fever, was evaluated using porcine skin as the sample. A novel conical MN design integrated with surface suction-cup structures was developed to improve tissue adhesion. Mechanical responses were analyzed through force–displacement measurements, evaluating insertion force, extraction force, and relaxation time. Results show that elevated tissue temperature reduces insertion and extraction forces while shortening relaxation times, indicating increased tissue compliance. The suction-cup MNs significantly enhanced needle-tissue adhesion, with the most pronounced effect observed in chicken breast tissue, achieving more than a 4-fold increase in extraction force compared to conventional conical needles. These findings provide valuable insights into optimizing the design of MNs for advanced biomedical applications.

Keywords: microneedles; tissue adhesion; drug delivery; biosensing; insertion force; extraction force

1. Introduction

Microneedles (MNs) are a promising class of transdermal delivery systems, offering numerous advantages over traditional methods [1]. Over three decades of research on MN-based drug delivery [2,3] and sensing [4,5] systems have demonstrated their potential to overcome challenges associated with conventional delivery techniques. Beyond their ease of administration, MNs provide additional benefits due to their unique interaction with the epidermis, which serves as the delivery pathway. The epidermis is rich in antigen-presenting cells (APCs), facilitating enhanced immune responses in applications such as vaccine delivery [6,7]. Moreover, MNs have shown significant promise in targeted and controlled drug release applications as well as in wearable biosensor technologies [8,9].

The development of MNs must adhere to specific criteria that align with their primary objectives: convenience and efficacy. Successful MN penetration serves as the foundation for practical MN applications, a characteristic that is consistent across various applications ranging from drug delivery to biosensing. One of the most critical yet often overlooked aspects is the needle-tissue interaction, which spans the entire process from initial insertion to full penetration and eventual extraction of the MN array. The needle-tissue interaction is a critical determinant of the system's overall performance. This knowledge enables the optimization of needle design for specific applications. A thorough

 doi:10.20944/preprints202506.2067.v1

understanding of this interaction leads to improved clinical outcomes, enhanced patient comfort, and reduced tissue damage.

Microneedle experiences a series of forces applied to the needle shaft during the insertion and removal procedures, i.e., insertion force and extraction force [10,11]. These forces must be maintained within a controlled range to minimize any potential issues arising from excessive force values. The insertion force refers to the force required for MNs to penetrate tissue. It should be minimized to reduce pain during application [12]. However, it must not be so low that it results in partial insertion, which could compromise the overall effectiveness of the process [13]. Extraction force refers to the force required to remove MNs after they have been used. This force should be sufficient to maintain reliable adhesion, particularly in applications that demand sustained contact with tissue [14–16], but must not exceed a threshold that compromises the convenience of the application [17].

The human body consists of various tissue types, each with distinct inherent properties, i.e., hydration, elasticity, and stiffness. Additionally, these tissue properties can change under both normal and extreme physiological conditions. These variations may influence the performance of MN insertion. Understanding these factors is essential for advancing personalized medicine, as the design of MNs and insertion conditions can be tailored to meet an individual's specific medical needs.

In the ongoing effort to optimize MN performance, numerous studies, both simulation-based and experimental, have explored enhancements in MN morphology [16,18–22] and material properties [23,24], primarily in the context of medical applications such as drug delivery. However, few studies have explored the fundamental mechanics of the needle-tissue penetration process. A deeper understanding of this process is essential for bridging the gap between device design and functional performance across diverse biological environments.

This study aims to present a different aspect of MN research, focusing on factors that influence needle-tissue interaction, with the primary objective of providing a framework for optimizing MNs. The insertion and extraction performance of a three-dimensional (3D) printed MN array was experimentally analyzed. Two main categories of influencing parameters were identified: internal factors, related to the properties of the target tissue (e.g., tissue type and temperature), and external factors, associated with the MN's structural characteristics and insertion conditions.

Figure 1 provides a schematic overview of the key parameters investigated in this study. Different tissue types, including chicken breast, pork skin, and agarose gel, have been selected as the tissue models, each resembling a specific body part. The effect of tissue temperature on needle-tissue interaction was analyzed across a range of physiologically relevant temperatures: room temperature (26 °C), body temperature (37 °C), hypothermia (32 °C), and fever conditions (42 °C). As part of external factors, a new shape of MN (a cone consisting of suction cups on the structure) has been proposed for tissue adhesion application. The effects of MN surface wettability and insertion velocity were also examined as other external influencing parameters. The aim of this study is to systematically assess the influence of each parameter on MN–tissue interaction, thereby informing future design strategies for more efficient and application-specific MN platforms.

 doi:10.20944/preprints202506.2067.v1

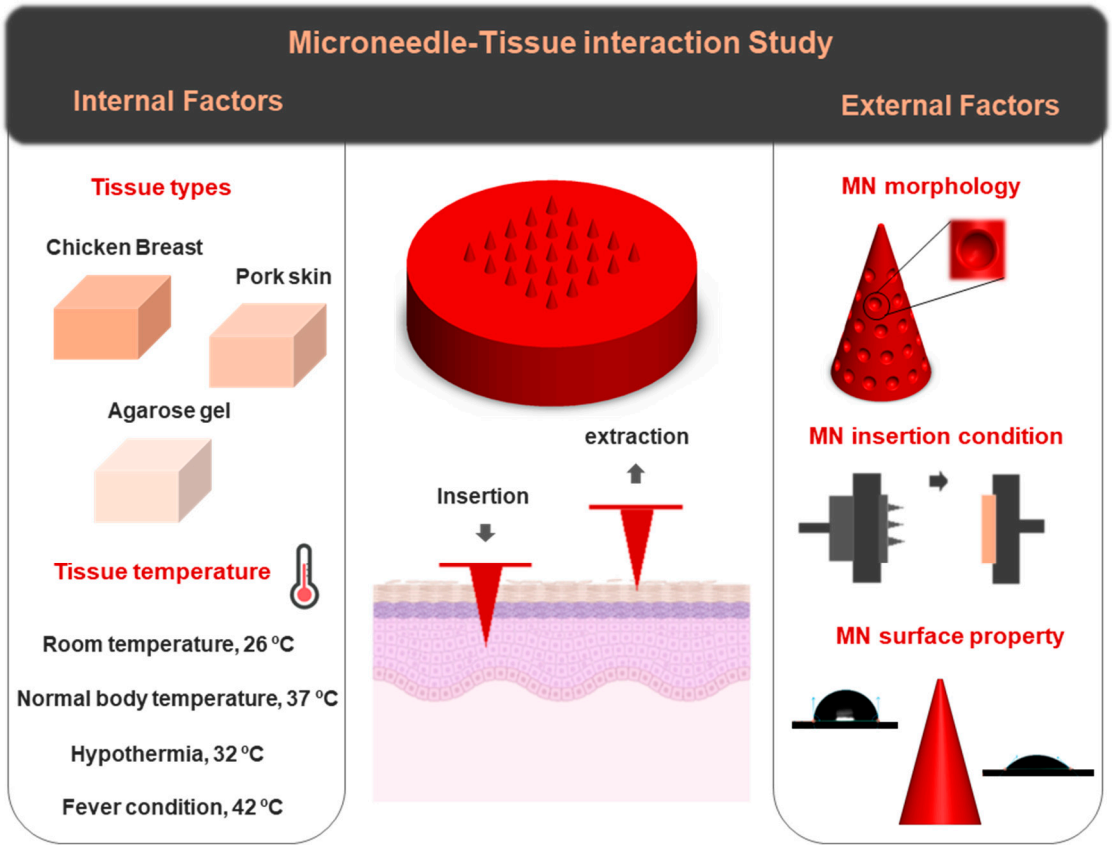

Figure 1. Schematic illustration of the experimental parameters investigated in this study, highlighting two major categories of factors influencing MN–tissue interactions: internal factors (tissue type and temperature) and external factors (MN morphology, insertion conditions, and surface properties). Tissue types include chicken breast, porcine skin, and agarose gel. Different temperatures (26°C, 32°C, 37°C, and 42°C) were tested for porcine skin to simulate physiological variations.

2. Materials and Methods

Materials: Tissue samples, chicken breast, and pork skin were purchased from a local butchery. Agarose (BioReagent, for molecular biology; low EEO, Sigma-Aldrich, St. Louis, MO) was used for the preparation of the non-fibrous tissue model. The tissue and MN patch holders were made of Poly (methyl methacrylate) (PMMA).

Equipment: A Boston microfabrication (BMF) S230 high-resolution digital light projection (DLP) 3D printer was used for the fabrication of MNs. Microneedles' surface morphology was analyzed using a scanning electron microscope (SEM) (Apreo 2S, Thermo Scientific, United States). Low vacuum mode was selected for imaging with a voltage of 20 kV and an amperage of 0.1 nA. The wettability of the patch material substrate was evaluated through water contact angle measurement using an optical tensiometer (Theta Flex, Biolin Scientific, Finland). A custom-built delaminator (DTS Company, 705 Wallea Drive, Menlo Park, CA) was used for MN insertion/extraction analysis. Plasma cleaner (PDC-002-CE, HARRICK PLASMA) was used to treat the simple conical MN patch and modify the surface chemistry of the needles. An ultrasonic cleaner (Model C1040) was used to regulate pork tissue temperature during experiments for tissue temperature effect analysis.

MN fabrication: Additive manufacturing of the devices was performed using a BMF S230 high-resolution DLD 3D printer. The BMF BIO resin used in this process was supplied by Embedded Logic Solutions Pty Ltd, Sydney, NSW. Photopolymerization was conducted using the S230's top-down projection system, operating at a maximum power density of 218.2 mW/cm², through a 50 μm-thick taut Fluorinated Ethylene Propylene (FEP) film. CAD 3D models were prepared using Voxeldance Additive Slicing software that allowed for modifying the layer thickness mid-print. This feature was used to optimize print times by adjusting layer thicknesses as needed to enhance surface feature

 doi:10.20944/preprints202506.2067.v1

resolution. The BMF S230 utilizes a ceramic roller to ensure the layer is printed to the programmed thickness. This is done by rolling the top of the FEP membrane before light projection for each layer. However, to prevent any possible damage to the small surface features and any damage to the FEP membrane, rolling was disabled for layers containing surface features.

During all 3D printing procedures, adequate dwell times according to BMF specifications were used to allow for the settling of turbulent resin and enhance layer accuracy.

Post-printing procedures included careful washing of all parts in filtered (Millipore, 0.45 μm) Propan-2-ol for 30 minutes, with solvent replacement. Once no resin residue remained, parts were allowed to air dry prior to post-print curing. Curing and annealing were carried out using a Formlabs Form Cure for 10 minutes, 50 °C, and 405 nm exposure.

Tissue sample preparation: A 2% agarose gel was prepared by dissolving 2 g of agarose powder in 100 mL of distilled water. First, the agarose powder was poured into a beaker, followed by the addition of the measured distilled water. The mixture was then heated in a microwave for 2 minutes until the powder was fully dissolved, resulting in a clear solution. After allowing the solution to cool, it was poured into a transparent polystyrene cube-shaped container for solidification. Pork skin and chicken breast were stored at 4 °C in a refrigerator immediately after purchase and used within 24 hours. Prior to testing, the tissues were removed from the fridge and allowed to thaw to room temperature, ensuring thermal equilibrium. The agarose gel, chicken breast, and pork skin were then trimmed into uniform pieces with dimensions of 3 cm × 3 cm.

Pork tissue preparation for temperature effect analysis: Pork skin tissue samples were prepared at defined temperatures to assess the influence of tissue temperature on MN performance. The tissue was placed in a glass beaker filled with water and immersed in an ultrasonic cleaner used solely as a temperature-controlled water bath. Importantly, the ultrasonic function was not activated during this process. The bath was set to the target temperature for each trial (26 °C, 32 °C, 37 °C, or 42 °C). The tissue remained in the chamber for 15 minutes to allow for temperature stabilization prior to testing.

MN insertion/extraction test: The tissue samples were mounted onto the moving stage of the delaminator setup by attaching them to a custom-fabricated poly(methyl methacrylate) (PMMA) holder. The MN patch was secured to the opposing stage, which was equipped with a load cell, using double-sided tape for a stable attachment to its corresponding PMMA holder. During testing, the tissue stage advanced toward the MN patch at a constant speed of 100 μm/s. After full insertion and completion of the relaxation period, the stage reversed direction, retracting the tissue at the same velocity to perform MN withdrawal.

Each test was repeated three times, and the results are reported as the mean ± standard deviation (SD).

3. Results and Discussion

3.1. Design Validation and Surface Morphology of MN

Two MN designs were developed for this study: a conventional smooth conical shape and a modified conical shape featuring regularly spaced hemispherical cavities intended to enhance tissue adhesion, Figure 2(a). Figure 2(b) presents the image of the fabricated MN array. The SEM images of the fabricated MNs are shown in Figure 2(c), (d). The general shape of the needles was successfully printed in a cone shape with base circle radius of 200 μm. Needle tips look sharp with a radius of 20 μm. The height of the MNs was chosen as 700 μm. The array contains 25 (5 × 5) needles in a square distribution pattern with needle interspacing of 1,000 μm.

 doi:10.20944/preprints202506.2067.v1

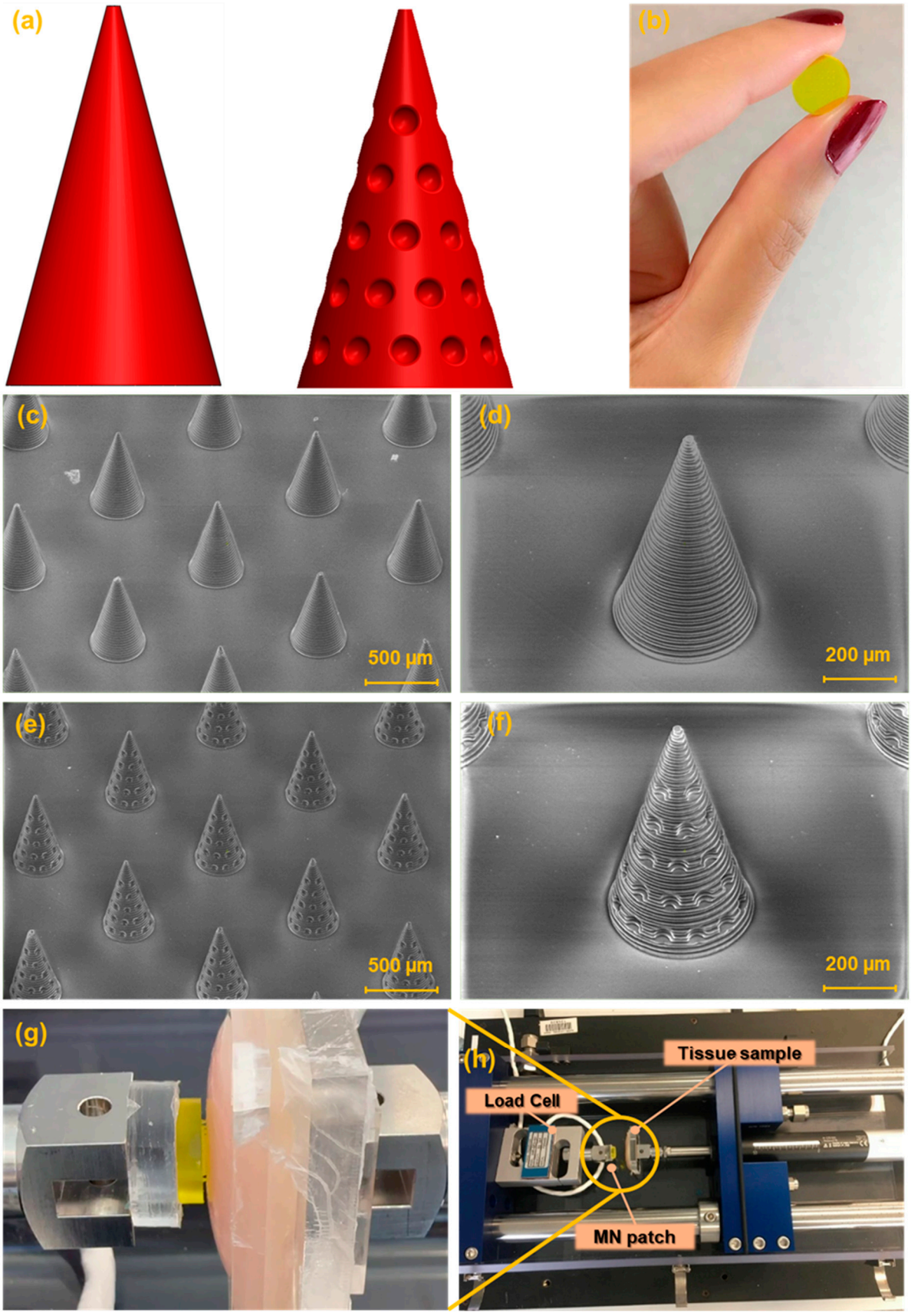

Figure 2. (a) Schematic of the CAD design of the simple conical MN and the new MN design (cone integrated with suction cup-like structures). (b) Image of 3D printed MN patch. SEM images of (c), (d) Simple conical MN array. (e), (f) New shape of MNs (Cone integrated with suction cups). (g), (h) image of the delaminator (setup of the experiment).

 doi:10.20944/preprints202506.2067.v1

3.2. Microneedle Insertion-Extraction Test

The mechanical performance of the MNs was evaluated using a custom-built platform based on a delaminator device, designed for force–displacement characterization (see Figure 2 (g), (h)). In the experimental setup, the tissue sample was securely affixed to the moving stage to prevent any undesired movement during testing. In contrast, the MN patch was mounted on a fixed stage equipped with a calibrated load cell to ensure accurate force measurements.

The moving stage was set to advance toward the fixed stage at a controlled speed of 100 μm/s, gradually bringing the tissue into contact with the needle tips. Upon initial contact, the system was reset, then the stage continued to move forward to allow full MN insertion into the tissue. Throughout this process, force–displacement data were collected using computer software, beginning from the moment of initial contact until complete needle insertion. The load cell recorded both loading and unloading forces, while the displacement was monitored via the position of the stage.

Figure 3(a) presents the force–displacement curve for MN penetration and extraction using chicken breast as the tissue model. The zero point on the graph represents the position where the needle tips first touch the tissue. The total needle displacement was set to 2,000 μm, which corresponds to approximately 2.8 times the needle height, ensuring full penetration and accounting for the elastic deformation of the tissue.

The stages of MN insertion and withdrawal are indicated on the graph. Stage 1 specifies the insertion stage. As the MN patch advances into the tissue, the applied force increases, reflecting the disruption of the tissue matrix and the need to overcome the mechanical resistance of internal structures. The maximum insertion force, measured once the MNs have fully penetrated the tissue, is recorded at 813 ± 4 mN.

After full insertion, the needles were left embedded in the tissue for a period defined as the relaxation or dwelling time (Stage 2). This phase allows for the assessment of the tissue's viscoelastic behavior, its time-dependent mechanical response to sustained deformation. Viscoelasticity encompasses two primary components: Elastic behavior, representing the tissue's ability to recover instantaneously upon load removal, and viscous behavior, which reflects a gradual, time-dependent deformation under constant stress.

During this phase, the force gradually decreases from its peak value and eventually stabilizes and reaches an equilibrium. This relaxation allows the tissue to conform around the MNs and adhere to their surfaces. The duration of this period tightly connects to the tissue properties. The recorded relaxation period for this case was 358 ± 5 s.

Following the relaxation period, the extraction phase begins (Stage 3). According to the force–displacement graph, the pull-out process starts from the equilibrium state after relaxation. This point is set as the origin of the extraction phase. The extraction force is calculated by subtracting the equilibrium force from the recorded force values during the extraction phase. As the patch is withdrawn, static friction between the tissue and MN surfaces causes a gradual increase in the extraction force. As seen in the graph, the slope is steeper at the initial stage, reaching the lowest point on the curve. The maximum extraction force required for MN detachment is 172 ± 5 mN. After the peak extraction force is reached, the force decreases as the MNs slide out of the tissue, eventually approaching zero.

 doi:10.20944/preprints202506.2067.v1

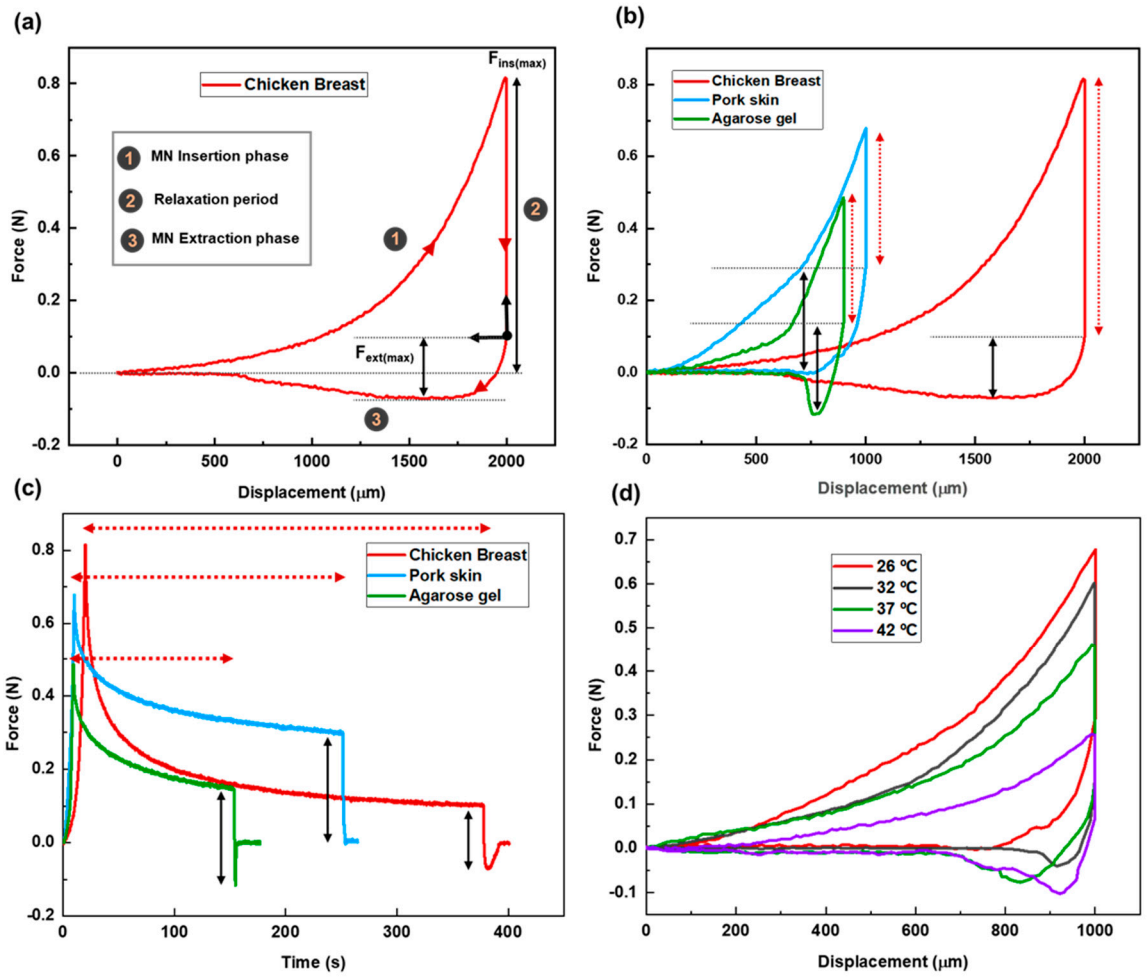

Figure 3. (a) Force-displacement graph for MN insertion/extraction test into chicken breast as the tissue model. (b) Force vs displacement graph for MN insertion/extraction test for three different tissues (chicken breast, pork skin, agarose gel) as representative of different human body parts. Red dashed lines and solid black lines represent relaxation period and maximum extraction force, respectively. (c) Force vs time graph for different tissues. Red dashed lines and solid black lines represent relaxation period and maximum extraction force, respectively. (d) Force-displacement graph for the pork skin as the tissue sample at different temperatures (26 ºC, 32 ºC, 37 ºC, 42 ºC) simulating different physiological conditions.

Overall, the force–displacement curve effectively illustrates the mechanical interaction between the MNs and the tissue throughout the entire insertion–dwell–extraction cycle. This behaviour is influenced by several factors, including internal parameters such as tissue composition, structure, and temperature, as well as external parameters such as MN geometry, material properties, and insertion velocity.

The following sections will provide a detailed discussion on how each of these factors influences MN–tissue interaction dynamics.

3.2.1. Internal (Tissue-Related) Factors

3.2.1.1. Comparative Analysis of MN Insertion–Extraction in Different Tissues

The MN insertion–extraction test was performed on three distinct tissue models: agarose gel, chicken breast, and pork skin. The corresponding force–displacement curves for each model are presented in Figure 3(b). Each tissue model was selected to mimic different types of human tissue: Agarose gel represents soft, hydrated tissues such as the human eye or wound sites. Chicken breast simulates soft muscle tissue. Pork skin serves as an analog for stiffer, more fibrous skin tissue.

 doi:10.20944/preprints202506.2067.v1

The insertion and extraction behavior of the MNs varied significantly across these tissue types, as reflected in key mechanical parameters, including insertion force, the required needle displacement for full insertion, relaxation time, and extraction force.

Based on their structural characteristics, the tissues were classified into two groups of fibrous tissues: Chicken breast and pork skin, and non-fibrous tissue: Agarose gel.

These structural differences were clearly visible in the force–displacement profiles (Figure 3(b)), with each tissue exhibiting a unique mechanical response to MN penetration and withdrawal. To ensure full MN penetration, displacement distances were tailored to each tissue's mechanical properties: Chicken breast: ~2,000 μm displacement, Pork skin: ~1,000 μm displacement, Agarose gel: ~900 μm displacement. These values were selected to guarantee full needle penetration.

During the insertion stage, the slope of the force–displacement curve for pork skin is the steepest, followed by agarose gel and then chicken breast. This indicates that the rate of force increase is highest for pork skin, which reflects its greater stiffness compared to other tested tissues.

Among the three tissue types, chicken breast exhibited the longest relaxation time (358 ± 5 s), indicating a strong viscous component and slower adaptation to MN insertion. Pork skin showed a moderate relaxation time (241 ± 3 s). Agarose gel had the shortest relaxation time (144 ± 6 s), suggesting a more elastic structure with a faster mechanical recovery following deformation. Figure 3(c) presents the force vs. time graph for the three cases, clearly illustrating the duration of the relaxation period (red dashed lines).

The overall force–displacement trends during the withdrawal process reveal an abrupt force transition in the agarose gel curve, implying a sudden structural failure and rapid response upon MN removal. In contrast, pork skin and chicken breast exhibit more gradual force changes during extraction. This behavior is likely attributed to the more elastic nature of agarose gel, in contrast to the viscoelastic characteristics of the biological tissues.

The relatively stiff nature of pork skin leads to a higher extraction force during MN removal compared to the softer tissues of agarose gel and chicken breast. The maximum extraction forces recorded for pork skin, chicken breast, and agarose gel are 298 ± 3, 172 ± 5, 234 ± 4 mN, respectively.

Table 1 presents the data regarding MN insertion and extraction processes for the three tested tissue samples.

Table 1. MN insertion/extraction key information for different tissue types. Each test was repeated three times, and the data are reported as mean ± SD.

Tissue type	MN displacement (μm)	Max insertion force (mN)	Relaxation period (s)	Max extraction force (mN)
Chicken breast	2000	813 ± 4	358 ± 5	172 ± 5
Pork skin	1000	664 ± 2	241 ± 3	298 ± 3
Agarose gel	900	471 ± 4	144 ± 6	234 ± 4

3.2.1.2. Tissue Temperature

In this section, we investigate the effect of tissue temperature on the mechanical interaction between MNs and tissue. Pork skin was chosen as the tissue model. A range of temperatures was applied to simulate different physiological conditions. Specifically, four temperature levels were tested: 26 °C (room temperature), 32 °C (hypothermic), 37 °C (normal body temperature), and 42 °C (febrile condition).

The force–displacement curves reveal that both insertion and extraction forces decrease as tissue temperature increases (see Figure 3(d)). This trend is attributed to enhanced molecular mobility at higher temperatures, which causes the tissue to soften and expand. As a result, MNs can more easily penetrate and withdraw from the tissue, requiring less force. The maximum insertion forces recorded

 doi:10.20944/preprints202506.2067.v1

were 664 ± 2 mN, 602 ± 2 mN, 458 ± 5 mN, and 258 ± 4 mN at 26 °C, 32 °C, 37 °C, and 42 °C, respectively. Correspondingly, the maximum extraction forces were 298 ± 3 mN, 198 ± 2 mN, 184 ± 3 mN, and 171 ± 4 mN for the same temperature conditions.

Temperature also influenced the relaxation time following MN insertion. Tissues at higher temperatures exhibited shorter relaxation periods. Since relaxation time serves as an indicator of the viscoelastic properties of tissue, and viscoelasticity is inversely related to temperature, this behavior suggests that warmer tissues adapt more quickly to the presence of MNs. Consequently, they display more elastic-like behavior under thermal conditions. Table 2 presents the data regarding MN insertion and extraction processes for the pork tissue at different temperatures.

Table 2. MN insertion/extraction key information for tissues with different temperatures. Each test was repeated three times, and the data are reported as mean ± SD (standard deviation).

Tissue temperature	Max insertion force (mN)	Relaxation period (s)	Max extraction force (mN)
Room temperature (26 ºC)	664 ± 2	241 ± 4	298 ± 3
Hypothermia (32 ºC)	602 ± 2	225 ± 2	198 ± 2
Normal body temperature (37 ºC)	458 ± 5	212 ± 4	184 ± 3
Fever condition (42 ºC)	258 ± 4	186 ± 2	171 ± 4

3.2.2. External Factors

In addition to the elements related to the nature of the tissue, there are other factors that require careful consideration, as they directly impact the needle-tissue interaction. These factors are primarily associated with external conditions, such as those related to the MN itself and the conditions governing the insertion process of the MN.

3.2.2.1. Microneedle Physical Morphology

As one of the primary factors that directly affect the needle-tissue interaction, the physical morphology of MNs significantly influences their insertion and extraction performance. This is especially evident in tissue adhesion applications, where the MN's ability to firmly anchor to tissue is essential. Among the various methods proposed so far as MN-tissue adhesion enhancers, morphological modifications have gained significant interest. Specific structural features incorporated into MN designs have been shown to enhance the extraction force [20], an essential metric for evaluating MN-tissue adhesion.

Building upon this concept, inspired by the suction cup structures found in octopus arms, biological features known for their strong adhesion, we developed a novel MN patch featuring conical MNs integrated with suction cup-like structures. This new design, illustrated in Figure 2(a) followed by its SEM images in Figure 2(e), (f), features a conical body integrated with 40 suction cups distributed across its surface. In addition to improved adhesiveness, this configuration offers a larger surface area compared to the simple conical counterpart—533,354 μm² versus 483,650 μm². The increased surface area also facilitates greater drug loading capacity, potentially enhancing drug delivery efficiency.

To evaluate the performance of this new design, comparative experiments were conducted using three tissue models: agarose gel, chicken breast, and pork skin. The corresponding force-displacement graphs are presented in Figure 4(a-c). Across all tissue types, MNs with suction cups demonstrated higher insertion forces, indicating increased resistance during penetration.

 doi:10.20944/preprints202506.2067.v1

Following insertion, tissues interacting with the suction cup design consistently displayed more extended relaxation periods, which is due to the additional time required for the tissue to accommodate the structural indentations.

The new MN design performed most effectively in chicken breast tissue, where a relatively modest increase in insertion force was accompanied by a substantial gain in extraction force. This suggests that the effectiveness of MN morphology in promoting tissue adhesion may be tissue-dependent. Therefore, MN design should be tailored to the specific properties of the target tissue, rather than adopting a one-size-fits-all approach. Table 3 presents the data regarding MN insertion and extraction processes for the new MN design for the three tested tissue samples.

Subsequently, higher extraction forces were recorded for the new design across all samples, confirming enhanced adhesion as a result of increased surface contact. A closer analysis of the force–displacement data reveals varying levels of adhesion response across tissue types. The relative increases in insertion and extraction forces between the simple and suction cup designs were as follows: Agarose gel: insertion force increased by 1.4×, extraction force by 1.134×. Pork skin: insertion force increased by 1.768×, extraction force by 2.01×. Chicken breast: insertion force increased by 1.6×, extraction force by 4.03×.

 doi:10.20944/preprints202506.2067.v1

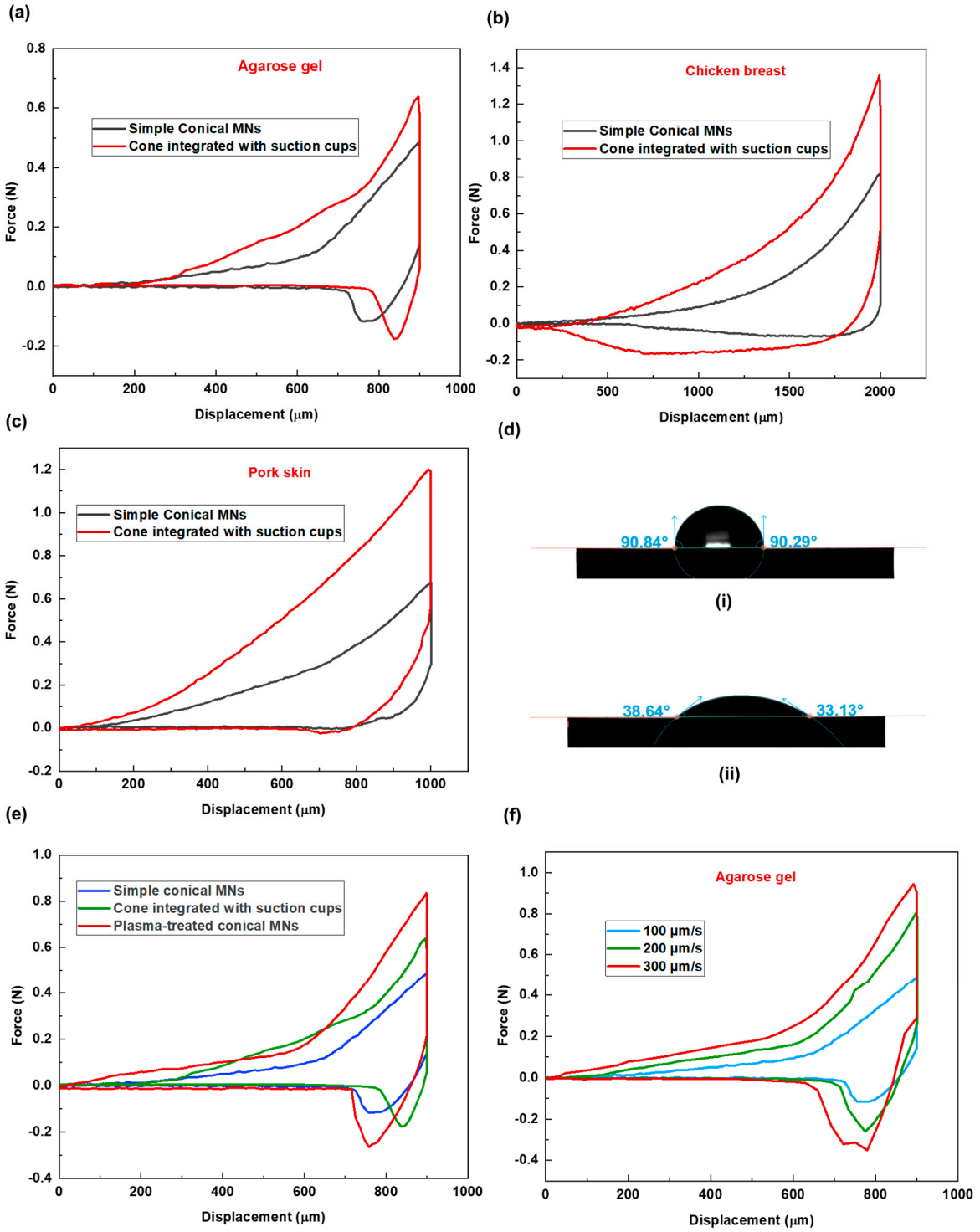

Figure 4. Force-displacement graphs for two MN shapes across three different tissues of (a) agarose gel, (b) chicken breast, and (c) pork skin. (d) Water contact angle measurement on (i) non-treated (ii) plasma-treated material substrate. (e) Force vs displacement graphs of simple conical, cone integrated with cup-like structures, and plasma-treated MNs demonstrating the effect of MNs surface treatment on needle-tissue mechanical behavior; the test was done for agarose gel as the tissue sample. (f) Force vs displacement graph demonstrating the effect of MNs insertion velocity on needle-tissue mechanical behavior; the test was done for agarose gel as the tissue sample.

Table 3. Microneedle insertion/extraction key characteristics for the new shape of the MNs cross different tissues. Each test was repeated three times, and the data are reported as mean ± SD.

 doi:10.20944/preprints202506.2067.v1

Tissue type	MN displacement (μm)	Max insertion force (mN)	Relaxation period (s)	Max extraction force (mN)
Chicken breast	2000	1334 ± 3	405 ± 2	689 ± 3
Pork skin	1000	1200 ± 5	363 ± 4	598 ± 3
Agarose gel	900	680 ± 5	194 ± 5	294 ± 4

3.2.2.2. Microneedle's Surface Chemical Property

Continuing our discussion on external factors influencing the behavior of MNs within tissue, we now focus on the chemical composition of MNs.

We decided to modify the chemical composition of MNs by applying plasma treatment to them. Contact angle measurement (Figure 4(d)) on the material substrate confirmed a significant increase in hydrophilicity following 15 s plasma treatment under low-pressure mode.

Following this, we conducted MN penetration tests in agarose gel, a tissue model with a high water content, 2% agarose gel (2g gel + 100 ml water). As shown in the force versus displacement graph (Figure 4(e)), there is a noticeable difference in the insertion and extraction phases for the treated MNs compared to the non-treated sample. The results demonstrated a further increase in tissue adhesion (higher extraction force), surpassing even the suction cup design. The maximum extraction force was 481 ± 2, 294 ± 4, and 234 ± 4 mN for the treated, suction-cup, and non-treated simple conical MNs, respectively. This enhanced adhesion is likely due to increased affinity between the MN surface and the agarose gel with a high water content. Furthermore, the comparatively longer relaxation period (264 ± 4 s) observed for the treated MNs is attributed to persistent MN–tissue surface molecular interactions.

These findings further highlight the importance of considering tissue composition when designing MNs. For example, in tissues with higher water content, such as wound tissues, this option of providing MNs with hydrophilic surface wetting property could function synergistically with the morphological modification aspect to further improve the system's efficacy.

Table 4 presents the data regarding MN insertion and extraction processes for the treated MNs, the new MN design, and the non-treated sample.

Table 4. MN insertion/extraction key characteristics for the non-treated conical MN, new shape, and plasma-treated MN patch in agarose gel as the tissue model. Each test was repeated three times, and the data are reported as mean ± SD.

MN type	MN displacement (μm)	Max insertion force (mN)	Relaxation period (s)	Max extraction force (mN)
Simple cone shape	900	471 ± 4	144 ± 6	234 ± 4
Cone integrated with suction cups	900	680 ± 5	194 ± 5	294 ± 4
Plasma-treated MNs	900	816 ± 4	264 ± 4	481 ± 2

3.2.2.3. Insertion Velocity

As an external factor influencing how MNs interact with tissue during insertion and extraction, the conditions under which MNs are inserted are also important. To this aim, three different insertion velocities of 100, 200, and 300 μm/s have been considered for the penetration study of solid conical MN patch in agarose gel. The graph of the MN insertion-extraction study shows differences in force-displacement values for these three cases (see Figure 4(f)). In that, higher insertion and extraction forces have been recorded for conditions with higher insertion velocity. This is because, at higher

 doi:10.20944/preprints202506.2067.v1

insertion velocities, the tissue becomes stiffer and more resistant to MN penetration due to insufficient time for relaxation. Similarly, the abrupt deformation caused by rapid insertion results in the needles becoming more tightly embedded in the tissue, thereby increasing the extraction force.

Table 5 presents the data regarding MN insertion and extraction processes for MN at different insertion velocities for the agarose gel tissue sample.

Table 5. MN insertion/extraction key characteristics for different insertion velocities for agarose gel tissue sample. Each test was repeated three times, and the data are reported as mean ± SD.

Insertion velocity	MN displacement (μm)	Max insertion force (mN)	Relaxation period (s)	Max extraction force (mN)
100 μm/s	900	471 ± 4	144 ± 6	234 ± 4
200 μm/s	900	779 ± 5	175 ± 3	527 ± 3
300 μm/s	900	943 ± 2	190 ± 4	641 ± 5

4. Conclusion

In this study, we investigated the factors influencing MN–tissue interactions, categorizing them into two main groups: internal factors, related to the tissue properties, and external factors, associated with MN design and insertion conditions. An MN patch was fabricated from bioresin material for this purpose. To evaluate internal factors, various tissues, i.e., pork skin, chicken breast, and agarose gel, were selected, each representing a different analog of human tissue. We also explored the effect of tissue temperature on MN performance by exposing the pork skin tissue sample to various conditions: room temperature (26°C), 32°C (hypothermia simulation), 37°C (normal body temperature), and 42°C (fever simulation).

For the external factors, we introduced a novel MN design with a conical shape featuring suction cup-like structures on its surface. The behavior of this new design was examined across the different tissue types. Additionally, we assessed the influence of MN surface wettability on tissue interaction and evaluated the effect of varying insertion velocities on penetration performance. Overall, our findings demonstrate that both tissue-specific properties and MN design characteristics significantly influence device behavior and can be optimized for clinical studies on MN-based platforms.

Data Availability Statement: The data that support the findings of this study are available from the corresponding author upon reasonable request.

Acknowledgements: This work was performed in part at the Queensland node of the Australian National Fabrication Facility (ANFF). A company established under the National Collaborative Research Infrastructure Strategy (NCRIS) to provide nano and microfabrication facilities for Australia's researchers. N.K. acknowledges funding support from the Australian Research Council (ARC) Discovery Early Career Research Award (DECRA) DE220100205 and ARC Linkage - Infrastructure (LIEF) LE230100078. N.-T.N. acknowledges funding support from the ARC Laureate Fellowship FL230100023.

Conflict of Interest: The authors declare no conflict of interest.

References

1. Sil, D.; Bhowmik, S.; Patel, P.; Kurmi, B.D. Promising role of MNs in therapeutic and biomedical applications. *Journal of Drug Delivery Science and Technology* **2024**, *91*, 105273.
2. Zheng, B.; Li, Q.; Liu, Y. Microorganism MN micro-engine depth drug delivery. Nat. Commun. 15, 8947 (2024).

 doi:10.20944/preprints202506.2067.v1

3. Chen, J.; Ren, H.; Zhou, P.; Zheng, S.; Du, B.; Liu, X.; Xiao, F. Microneedle-mediated drug delivery for cutaneous diseases. *Frontiers in Bioengineering and Biotechnology* **2022**, *10*, 1032041.
4. Madden, J.; O'Mahony, C.; Thompson, M.; O'Riordan, A.; Galvin, P. Biosensing in dermal interstitial fluid using MN based electrochemical devices. Sens Bio-Sensing Res 29: 100348. **2020**.
5. Zeng, Q.; Xu, M.; Hu, W.; Cao, W.; Zhan, Y.; Zhang, Y.; Wang, Q.; Ma, T. Porous colorimetric MNs for minimally invasive rapid glucose sampling and sensing in skin interstitial fluid. *Biosensors* **2023**, *13*, 537.
6. Weldon, W.C.; Martin, M.P.; Zarnitsyn, V.; Wang, B.; Koutsonanos, D.; Skountzou, I.; Prausnitz, M.R.; Compans, R.W. Microneedle vaccination with stabilized recombinant influenza virus hemagglutinin induces improved protective immunity. *Clinical and Vaccine Immunology* **2011**, *18*, 647-654.
7. Chopra, A.; Gupta, A. Skin as an immune organ and the site of biomimetic, non-invasive vaccination. *Medicine in Novel Technology and Devices* **2022**, *16*, 100196.
8. Tehrani, F.; Teymourian, H.; Wuerstle, B.; Kavner, J.; Patel, R.; Furmidge, A.; Aghavali, R.; Hosseini-Toudeshki, H.; Brown, C.; Zhang, F. An integrated wearable MN array for the continuous monitoring of multiple biomarkers in interstitial fluid. *Nature Biomedical Engineering* **2022**, *6*, 1214-1224.
9. Xie, Z.; Zhang, X.; Chen, G.; Che, J.; Zhang, D. Wearable MN-integrated sensors for household health monitoring. *Engineered Regeneration* **2022**, *3*, 420-426.
10. Cheung, K.; Han, T.; Das, D.B. Effect of force of MN insertion on the permeability of insulin in skin. *Journal of diabetes science and technology* **2014**, *8*, 444-452.
11. Davis, S.P.; Landis, B.J.; Adams, Z.H.; Allen, M.G.; Prausnitz, M.R. Insertion of MNs into skin: measurement and prediction of insertion force and needle fracture force. *Journal of biomechanics* **2004**, *37*, 1155-1163.
12. Kim, J.; Jeong, J.; Jo, J.K.; So, H. Hollow MNs as a flexible dosing control solution for transdermal drug delivery. *Materials Today Bio* **2025**, 101754.
13. Makvandi, P.; Kirkby, M.; Hutton, A.R.; Shabani, M.; Yiu, C.K.; Baghbantaraghdari, Z.; Jamaledin, R.; Carlotti, M.; Mazzolai, B.; Mattoli, V. Engineering MN patches for improved penetration: analysis, skin models and factors affecting needle insertion. *Nano-Micro Letters* **2021**, *13*, 1-41.
14. Liu, T.; Sun, Y.; Jiang, G.; Zhang, W.; Wang, R.; Nie, L.; Shavandi, A.; Yunusov, K.E.; Aharodnikau, U.E.; Solomevich, S.O. Porcupine-inspired MNs coupled with an adhesive back patching as dressing for accelerating diabetic wound healing. *Acta biomaterialia* **2023**, *160*, 32-44.
15. Haghniaz, R.; Kim, H.-J.; Montazerian, H.; Baidya, A.; Tavafoghi, M.; Chen, Y.; Zhu, Y.; Karamikamkar, S.; Sheikhi, A.; Khademhosseini, A. Tissue adhesive hemostatic MN arrays for rapid hemorrhage treatment. *Bioactive Materials* **2023**, *23*, 314-327.
16. Lim, S.; Park, T.Y.; Jeon, E.Y.; Joo, K.I.; Cha, H.J. Double-layered adhesive MN bandage based on biofunctionalized mussel protein for cardiac tissue regeneration. *Biomaterials* **2021**, *278*, 121171.
17. Lori Zoudani, E.; Nguyen, N.T.; Kashaninejad, N. Microneedle optimization: Toward enhancing MN's functionality and breaking the traditions. *Small Structures* **2024**, *5*, 2400121.
18. Li, W.; Terry, R.N.; Tang, J.; Feng, M.R.; Schwendeman, S.P.; Prausnitz, M.R. Rapidly separable MN patch for the sustained release of a contraceptive. *Nature Biomedical Engineering* **2019**, *3*, 220-229.
19. Huang, D.; Fu, X.; Zhang, X.; Zhao, Y. Christmas tree-shaped MNs as FOLFIRINOX spatiotemporal delivery system for pancreatic cancer treatment. *Research* **2022**.
20. Han, D.; Morde, R.S.; Mariani, S.; La Mattina, A.A.; Vignali, E.; Yang, C.; Barillaro, G.; Lee, H. 4D printing of a bioinspired MN array with backward - facing barbs for enhanced tissue adhesion. *Advanced Functional Materials* **2020**, *30*, 1909197.
21. Yang, P.; Song, Q.; Zhang, L.; Liu, Z.; Ma, H. Numerical modeling and simulation for MNs drug delivery: A novel comprehensive swelling-obstruction-mechanics model. *European Journal of Pharmaceutics and Biopharmaceutics* **2025**, *206*, 114583.
22. Zoudani, E.L.; Soltani, M. A new computational method of modeling and evaluation of dissolving MN for drug delivery applications: Extension to theoretical modeling of a novel design of MN (array in array) for efficient drug delivery. *European Journal of Pharmaceutical Sciences* **2020**, *150*, 105339.

 doi:10.20944/preprints202506.2067.v1

23. Yang, Z.-R.; Suo, H.; Fan, J.-W.; Lv, N.; Du, K.; Ma, T.; Qin, H.; Li, Y.; Yang, L.; Zhou, N. Endogenous stimuli-responsive separating MNs to inhibit hypertrophic scar through remodeling the pathological microenvironment. *Nature Communications* **2024**, *15*, 2038.
24. Qi, Z.; Yan, Z.; Tan, G.; Kundu, S.C.; Lu, S. Smart responsive MNs for controlled drug delivery. *Molecules* **2023**, *28*, 7411.